Inorganic Chemistry

Article

pubs.acs.org/IC

Ferric Complexes of 3-Hydroxy-4-pyridinones Characterized by Density Functional Theory and Raman and UV−vis Spectroscopies

Jaroslav Šebestík,* Martin Šafařík, and Petr Bouř

Institute of Organic Chemistry and Biochemistry, Academy of Sciences of the Czech Republic, Flemingovo náměstí 2, 16610 Prague, Czech Republic

Supporting Information

ABSTRACT: Deferiprone and other 3-hydroxy-4-pyridinones are used in metal chelation therapy of iron overload. To investigate the structure and stability of these compounds in the natural aqueous environment, ferric complexes of deferiprone and amino acid maltol conjugates were synthesized and studied by computational and optical spectroscopic methods. The complexation caused characteristic intensity changes, a 300× overall enhancement of the Raman spectrum, and minor changes in UV−vis absorption. The spectra were interpreted on the basis of density functional theory (DFT) calculations. The CAM-B3LYP and ωB97XD functionals with CPCM solvent model were found to be the most suitable for simulations of the UV−vis spectra, whereas B3LYP, B3LYPD, B3PW91, M05-2X, M06, LC-BLYP, ωB97XD, and CAM-B3LYP functionals were all useful for simulation of the Raman scattering. Characteristic Raman band frequencies for 3-hydroxy-4-pyridinones were assigned to molecular vibrations. The computed conformer energies consistently suggest the presence of another isomer of the deferiprone-ferric complex in solution, in addition to that found previously by X-ray crystallography. However, the UV−vis and Raman spectra of the two species are similar and could not be resolved. In comparison to UV−vis, the Raman spectra and their combination with calculations appear more promising for future studies of iron sequestrating drugs and artificial metalloproteins as they are more sensitive to structural details.

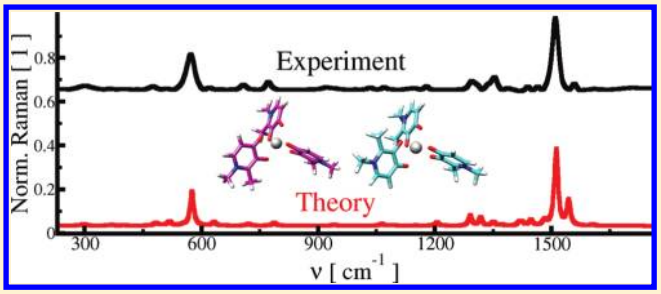

INTRODUCTION

Iron-specific chelators (ISC) are efficient drugs for clinical treatment of the pathological iron overload.[1] ISC could be used to cure the neurodegenerative processes such as Alzheimer's, Parkinson's, and prion diseases,[2,3] where the iron plays a significant role.[4,5] Humans cannot easily eliminate the iron, and a homeostasis is maintained by the regulation of iron uptake.[1] In healthy individuals, tight control of iron level prevents productions of free radicals via iron catalyzed Fenton's reaction.[6]

Iron sequestrating agents are designed as hard chelators,[1] because soft chelators could reduce levels of other essential bivalent metals, such as copper(II) and zinc(II). Bi-, tri-, and hexadentate ligands provide the most stable octahedral arrangement for iron(III). For example, formation of kinetically inert complexes of hexadentate ligands with ferric ion prevents iron redistribution.[7]

The derivatives of the 3-hydroxy-4-pyridinone (3,4-HP) investigated in this work are also used as drugs for treatment of iron overload; additionally, they may be efficient against bacterial infections,[8] and the Alzheimer's and Parkinson's diseases.[3] In particular, the Deferiprone (3-hydroxy-1,2-dimethylpyridin-4(1*H*)-one) was approved by the European Medicines Evaluation Agency for treatment of iron overload (EU/1/99/108/001) and sickle cell disease (EMA/COMP/740288/2010). Clinical trials are also carried out in the U.S.A. (http://clinicaltrials.gov/ct2/show/NCT00293098). Bidentate conjugates of peptides with 3,4-HPs were used as artificial siderophores.[9] Previously, we have shown that hexadentate conjugates of 2-methyl-3,4-HPs with Kemp's acid and diamine linkers are powerful ISCs.[10] Because of powerful sequestration of iron and ^{67}Ga, these conjugates can be used in metal-chelation therapy. Conjugates with peptides, glycopeptides, and dendrimers are used in imaging techniques, drug delivery, and cancer therapy.[11−13]

To rationalize the design of the sequestrating agents, we studied structure and spectroscopic properties of ferric 3,4-HPs complexes in solution. With few exceptions, the dendrimeric complexes of 3,4-HPs cannot be crystallized.[11,13] Additionally, the solution structure may not correspond to a crystal. The ferric ion is paramagnetic in a high-spin state, and nuclear magnetic resonance (NMR) can provide only limited information about the complexes.[14] Thus we use the Raman and UV−vis spectroscopies to verify the computational predictions of the structure. Especially vibrational spectroscopy in combination with density functional theory (DFT) is known to provide detailed information about molecular structure in solutions.[15−17]

Received: September 13, 2011
Published: April 2, 2012

There are limited possibilities to predict theoretically the structure of the complexes by molecular dynamics (MD). For ferric hexadentate complexes the MD-derived geometries correlated with the crystal structures.[18] However, for other ligands with high steric hindrances geometries obtained by DFT were different from those obtained by MD.[10]

DFT calculations provide a more universal way of predicting properties of ferric complexes than MD.[19] However, a proper solvent model is needed for reliable results.[20,21] The catechol binding to porphyrin iron complex was recently calculated by DFT.[22] Relativistic corrections were incorporated by using a pseudo potential on the iron atom,[23] although they did not appear important for this case. For example, nitric oxide binding to the heme groups was investigated with the LACV3P basis set on iron and the 6-31G* basis set on other atoms.[24]

Occasionally, comparisons of the DFT calculations with CCSD(T) results revealed that the energetics of iron NO complexes may be incorrectly predicted by DFT.[24] In most cases, however, the DFT provides satisfactory results.[10] For the spectroscopic methods the DFT computational predictions are extremely useful to interpret the spectra, and usually provide good accuracy. For Fe-catecholate and Fe-oxalate, IR vibrational transitions[25] were calculated with error of 11 cm^{-1} in the region of 1600−700 cm^{-1}. Resonance Raman spectroscopy and DFT modeling have been used for explanation of nitric oxide bonding in Fe(III) heme proteins.[26] The Raman spectroscopy is especially convenient for aqueous solutions as it allows to study the biologically relevant complexes in the natural environment. The time scale of the optical methods is also shorter than for NMR, which in principle allows for resolution of more conformers.[15,17,27−29]

In this work, we report the measurement and analysis of UV−vis and Raman spectra of a ferric complex of deferiprone as a model of 3,4-HP chelator. The geometry, complex stability, and conformations (isomers) are estimated by DFT, using the polarizable continuum solvent model. The importance of the basis set size, pseudo potential, functional, and solvent environment for the computational design of peptide-based ISCs is discussed. As shown below the combined computational and spectroscopic approach can reveal new isomers of the complexes, unseen by X-ray crystallography, which are also more relevant to the structure in vivo.

EXPERIMENTAL SECTION

General Procedures. The chemical reactions were monitored by thin-layer chromatography (TLC) using aluminum plates coated with silica gel 60 F254 (Merck). TLC detection methods were used: UV 254 nm, staining with I2 (general), ninhydrin (for amino groups), and Dragendorff's reagent (for pyridinones). The common mobile phases were used: A0 ($CHCl_3$: MeOH 9:1); A1 (CH_3CN: 24% NH_4OH 2:1). The synthesized derivatives were characterized by high-performance liquid chromatography (HPLC; Agilent 1200 instrument with quaternary pump, thermostat, diode array detector and reverse phase Poroshell 120SB-C_{18} 2.7 μm, 3 × 50 mm column; gradient 5−18−100% CH_3CN for 0−10−15 min using 0.05% TFA in mobile phase); by ^1H and ^{13}C nuclear magnetic resonance spectroscopy (^1H and ^{13}C NMR; Bruker Avance I, 400 MHz instrument); and by electrospray ionization mass spectroscopies with high resolution (ESI-HRMS Waters Q-Tof micro instruments). Raman and ROA spectra acquired with a commercial BioTools ChiralRAMAN-2X instrument (532 nm excitation wavelength, 128 scans, 1.03 s illumination time, concentration 4 mg/mL for high ligand to metal ratios down to 0.04 mg/mL for low ligand to metal ratios, laser power at the sample 462 mW, the absorbance of laser was maintained below 2 by sample dilution) were processed using homemade software.[30] UV−vis spectra were collected using Perkin-Elmer Lambda 25 instrument.

Synthesized Compounds. *3-Benzyloxy-2-methyl-4H-pyran-4-one (1).* The synthesis was adapted according to Green et al.[31] Yield 91%. TLC R_F (A0) 0.93; R_F (DCM) 0.12. ^1H NMR (400 MHz, $CDCl_3$): δ 7.59 (d, 1H, 5.6 Hz, C_{ar}-H_6), 7.36 (m, 5H, Ph-H), 6.35 (d, 1H, 5.6 Hz, C_{ar}-H_5), 5.15 (s, 2H, $-CH_2-$Ph), 2.09 (s, 3H, Py-CH_3). ^{13}C NMR (100 MHz, $CDCl_3$): δ 175.1 (**C**=O), 159.7 (**C**-O_1), 153.5 (**C**H$-O_1$), 143.9 (**C**-O$-CH_2$), 137.0 (C-ipso Ph), 129.1 (C_{Ph}−H), 128.5 (C_{Ph}−H), 128.4 (C_{Ph}−H), 117.3 (**C**H−CO), 73.7 (**C**H_2), 14.9 (**C**H_3).

3-Benzyloxy-1,2-dimethyl-1H-pyridin-4-one Hydrochloride (2). The compound was synthesized according to combined procedures of Dobbin et al.[32] and Liu et al.[33] Yield 75%. Mp 207−210 °C (207−208 °C;[32]). ^1H NMR (400 MHz, D_2O): δ 8.12 (d, 1H, 7.1 Hz, C_{ar}-H_6), 7.41 (m, 5H, Ph-H), 7.11 (d, 1H, 7.1 Hz, C_{ar}-H_5), 5.10 (s, 2H, $-CH_2-$Ph), 3.90 (s, 3H, N$-CH_3$), 2.37 (s, 3H, C$-CH_3$).

Deferiprone (3). The compound **2** was released from its salt by 2 M NaOH. After washing with DCM and drying with Na_2SO_4, the organic layer was evaporated to dryness. A hydrogenolysis was carried out according to Rumbo et al.[34] Yield 80%. Mp 222−224 °C (272−276 °C;[34]). TLC R_F (A1) 0.52. HPLC RT 0.35 min. ^1H NMR (400 MHz, dmso-d_6): δ 8.15 (d, 1H, 6.9 Hz, C_{ar}-H_6), 7.07 (d, 1H, 6.9 Hz, C_{ar}-H_5), 3.95 (s, 3H, N$-CH_3$), 2.47 (s, 3H, C$-CH_3$). ^{13}C NMR (100 MHz, dmso-d_6): δ 159.7 (**C**=O), 143.0 (**C**−OH), 140.7 (**C**-CH_3), 138.5 (**C**H−N), 110.3 (**C**H−CO), 43.6 (N-**C**H_3), 12.5 (C-**C**H_3). For $C_7H_{10}NO_2$ (140.07061) found ESI-HRMS, m/z: 140.07054 ($M+H^+$); −0.484 ppm.

δ-(3-Benzyloxy-1,4-dihydro-2-methyl-4-oxo-1-pyridyl)-L-norvaline (4). The procedure used was adapted from Santos et al.[35] To the compound **1** (1.6 g, 7.5 mmol) and HCl·H-Orn-OH (1.2 g, 7.12 mmol) in methanol−water (60 mL, 1:1) was added 10% NaOH until pH 13 was reached. The mixture was heated under reflux overnight and then evaporated to dryness. The residuum was redissolved in a mobile phase (CH_3CN:25% NH_4OH (7:1)) and separated by flash column chromatography on silicagel. After evaporation and vacuum drying, the yield was 9%. Mp 178−182 °C (141−142 °C;[35]). TLC R_F (A1) 0.47. HPLC RT 4.0 min. ^1H NMR (400 MHz, D_2O): δ 7.67 (d, 1H, 7.5 Hz, C_{ar}-H_6), 7.36 (m, 5H, Ph-H), 6.16 (d, 1H, 7.5 Hz, C_{ar}-H_5), 4.99 (s, 2H, $-CH_2-$Ph), 3.89 (t, 2H, 6.5 Hz, δ-CH_2), 3.24 (t, 1H, 5.5 Hz, α-CH), 2.19 (s, 3H, Py-CH_3), 1.69 (m, 4H, β-CH_2, γ-CH_2). For $C_{18}H_{21}N_2O_4$ (329.15068) found ESI-HRMS, m/z: 329.15063 ($M+H^+$); −0.141 ppm.

δ-(3-Hydroxy-1,4-dihydro-2-methyl-4-oxo-1-pyridyl)-L-norvaline (5). Adapted procedure from Santos et al.;[35] instead of Pd/C, a Pd sponge was used. Mp 192−195 °C (172−174 °C;[35]). TLC R_F (A1) 0.13. HPLC RT 0.35 min. ^1H NMR (400 MHz, D_2O): δ 7.77 (d, 1H, 7.0 Hz, C_{ar}-H_6), 6.65 (d, 1H, 7.0 Hz, C_{ar}-H_5), 4.21 (t, 2H, 7.0 Hz, δ-CH_2), 3.77 (t, 1H, 5.8 Hz, α-CH), 2.49 (s, 3H, Py-CH_3), 1.93 (m, 4H, β-CH_2, γ-CH_2). For $C_{11}H_{15}N_2O_4$ (239.10373) found ESI-HRMS, m/z: 239.10380 ($M+H^+$); +0.303 ppm.

ε-(3-Benzyloxy-1,4-dihydro-2-methyl-4-oxo-1-pyridyl)-L-norleucine (6). Procedure similar as for the sodium salt.[9] The purification was achieved by the same column chromatography as for compound **4**. Mp 152−156 °C. TLC R_F (A1) 0.48. HPLC RT 5.1 min. ^1H NMR (400 MHz, dmso-d_6): δ 7.67 (d, 1H, 7.4 Hz, C_{ar}-H_6), 7.37 (m, 5H, Ph-H), 6.17 (d, 1H, 7.4 Hz, C_{ar}-H_5), 4.99 (s, 2H, $-CH_2-$Ph), 3.85 (t, 2H, 7.2 Hz, ε-CH_2), 3.22 (t, 1H, 5.3 Hz, α-CH), 2.15 (s, 3H, Py-CH_3), 1.69 (m, 2H, β-CH_2), 1.54 (m, 2H, δ-CH_2), 1.34 (m, 2H, γ-CH_2). For $C_{19}H_{23}N_2O_4$ (343.16633) found ESI-HRMS, m/z: 343.16617 ($M+H^+$); −0.477 ppm.

ε-(3-Hydroxy-1,4-dihydro-2-methyl-4-oxo-1-pyridyl)-L-norleucine (7). A product of hydrogenolysis as described above. Mp 185−190 °C. TLC R_F (A1) 0.20. HPLC RT 0.30 min. ^1H NMR (400 MHz, D_2O): δ 7.75 (d, 1H, 7.1 Hz, C_{ar}-H_6), 6.65 (d, 1H, 7.1 Hz, C_{ar}-H_5), 4.16 (t, 2H, 7.5 Hz, ε-CH_2), 3.71 (t, 2H, 6.1 Hz, α-CH), 2.46 (s, 3H, Py-CH_3), 1.85 (m, 4H, β-CH_2, δ-CH_2), 1.37 (m, 2H, γ-CH_2). For $C_{12}H_{17}N_2O_4$ (253.12938) found ESI-HRMS, m/z: 253.11935 ($M+H^+$); −0.137 ppm.

dx.doi.org/10.1021/ic202004d | Inorg. Chem. 2012, 51, 4473−4481

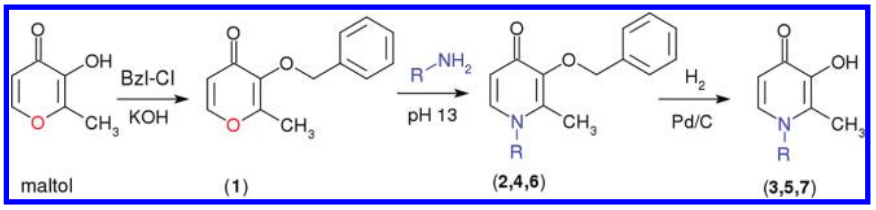

Figure 1. Scheme of synthesis of 3-hydroxy-4-pyridinones.[59] R stands for CH_3 (**2**, **3**); $CH_2CH_2CH_2CH(COOH)(NH_2)$ (**4**, **5**); and $CH_2CH_2CH_2CH_2CH(COOH)(NH_2)$ (**6**, **7**).

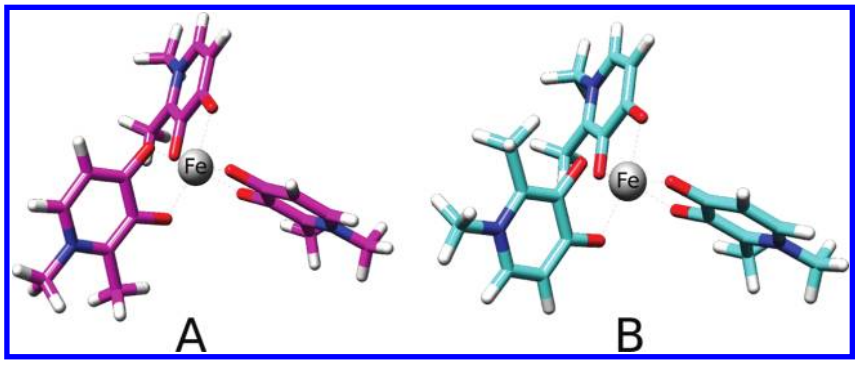

Figure 2. Two isomers of the deferiprone ferric complex. **A** is symmetrical one (C3 point group); the nonsymmetrical (C_1) isomer **B** can be obtained by a 180° rotation of 3,4-HP from **A**.

Computations. The geometry optimizations and computations of the Raman and UV–vis spectra were done with the Gaussian program,[36] using the B3LYP,[37−40] B3PW91,[41,42] B97D,[43] CAM-B3LYP,[44] B3LYPD,[45,46] M05-2X,[47] M06,[48] LC-BLYP,[49] and ωB97XD[50,51] functionals, 6-31+G** and 6-311++G** standard basis sets, MDF10 pseudopotential,[52−54] and the CPCM[55−57] solvent model (which is the Gaussian implementation of the COSMO model[58]). Calculated UV–vis intensities were convoluted with Gaussian functions (full width at half height (fwhh) was usually 25 nm, as specified below); in the case of Raman spectra Lorentzian functions were used (fwhh 10 cm^{-1}).

RESULTS AND DISCUSSION

Synthesis. 3-Hydroxy-4-pyridinones were synthesized following the known procedure in Figure 1.[59] First, hydroxyl group of maltol was protected with benzyl chloride. A heterocyclic nitrogen was introduced by opening of the 4-pyrone ring (**1**), and subsequent closure of the pyridinone one (**2**, **4**, **6**). Removal of the protection group provided 3-hydroxy-4-pyridinone derivatives (**3**, **5**, **7**) by the catalytic hydrogenolysis.

Conformational Analysis. Two stable geometries of complexes of deferiprone with iron(III) were found by the DFT computations (**A**, **B**, cf. Figure 2). Only the **A**-isomer of the complex was previously identified by X-ray crystallography.[60] The **A**:**B** conformer ratio was predicted to be approximately 6:4 in vacuum (Table 1; items 1−3,7,8,12,13), as well as, in the water simulated by the CPCM model (Table 1; items 4−6,9−11,14−22). The absence of **B** conformer in the X-ray analysis can be attributed to the crystal packing forces not included in the calculations.

The **A**/**B** isomer populations as calculated by different theoretical models are listed in Table 1. The change of the Fe core electrons by the pseudopotential or the 6-311++G** - 6-31+G** basis set variation do not change the **A**/**B** ratio significantly (cf. Items 1,2,4,5,9,10,14,15,17 and 18, Table 1). The addition of the water environment via the CPCM model only slightly stabilizes **A**.

UV–vis Spectrum of M/L 1:3 Complex. The dependence of the absorption maximum on the ratio of deferiprone to ferric cation enabled us to find the optimal concentrations for measurement (in Supporting Information, Figure S1). Since the spectrum at the metal to ligand charge transfer (MLCT) region became constant for the ratio above 10:1, the ratio 20:1 of deferiprone to ferric cation was used for comparison of experimental and calculated spectra. At these conditions all the iron should be bound in the complex; the free deferiprone ligand is not visible in the relevant spectral part.

Most of the examined DFT functionals, with exception of CAM-B3LYP, overestimated the wavelength of the MLCT band. The experimental spectrum (Figure 3, black line) is very close to those simulated at the CAM-B3LYP/6-311++G**/CPCM level (red lines). Uncorrected B3LYP overestimates the wavelength. The B3PW91 functional provides the absorption maximum closer by ∼30 nm to the experiment, but still rather far from the desired value of 456 nm. The pseudopotential had a minor (an 8 nm shift) effect on the B3LYP simulated spectra. The position of B3PW91 simulated maximum was kept unchanged by the pseudopotential; however, the intensities were slightly altered (cf Figure 3 and Supporting Information, Figure S2). The CAM-B3LYP spectra were slightly improved by application of the pseudopotential. The absorption maximum moved from 472 to 461 nm, that is, an 11 nm closer to the experimental value (Figure 3 and Supporting Information, Figure S2). The long-range ωB97XD functional with dispersion correction and the same basis set and pseudopotential predicted the maximum at 466 nm, that is, slightly further from experiment than CAM-B3LYP. The relatively large experimental band broadening (fwhh = 82 nm) is caused by interaction between the solute and the solvent molecules.[61] Such inhomogeneous broadening would require calculations with explicit solvent and accounting for molecular dynamics,[62] which would be, however, unreasonably more time demanding than the CPCM computations (requiring them-

dx.doi.org/10.1021/ic202004d | Inorg. Chem. 2012, 51, 4473−4481

Table 1. Boltzmann Weights of Isomers A and B (Figure 2) at 300 K Calculated with Several DFT Functionals and Basis Sets

item	method	isomer A [%]	isomer B [%]
	B3LYP		
1	6-31+G**; Fe with 6-311++G**	58	42
2	6-31+G**; Fe with MDF10.	59	41
3	all with 6-311++G**	57	43
4	6-31+G**; Fe with 6-311++G**, CPCM	58	42
5	6-31+G**; Fe with MDF10, CPCM	60	40
6	all with 6-311++G**, CPCM	60	40
	B3PW91		
7	6-31+G**; Fe with 6-311++G**	56	44
8	all with 6-311++G**	58	42
9	6-31+G**; Fe with 6-311++G**, CPCM	57	43
10	6-31+G**; Fe with MDF10, CPCM	58	42
11	all with 6-311++G**, CPCM	60	40
	B97D		
12	6-31+G**; Fe with 6-311++G**	58	42
13	all with 6-311++G**	58	42
14	6-31+G**; Fe with 6-311++G**, CPCM	64	36
15	6-31+G**; Fe with MDF10, CPCM	62	38
16	all with 6-311++G**, CPCM	63	37
	CAM-B3LYP		
17	6-31+G**; Fe with 6-311++G**, CPCM	60	40
18	6-31+G**; Fe with MDF10, CPCM	61	39
19	all with 6-311++G**, CPCM	63	37
	B3LYPD		
20	6-31+G**; Fe with MDF10, CPCM	64	36
	M05-2X		
21	6-31+G**; Fe with MDF10, CPCM	57	43
	M06		
22	6-31+G**; Fe with MDF10, CPCM	64	36
	LC-BLYP		
23	6-31+G**; Fe with MDF10, CPCM	62	38
	ωB97XD		
24	6-31+G**; Fe with MDF10, CPCM	58	42

selves average simulation time of about 28 CPU days at 2 GHz).

The UV–vis spectra clearly do not allow to discriminate the A and B isomers. The minor differences (shoulder at 403 nm, Figure 3) cannot be distinguished because of the broadening. Nevertheless, we see that the CAM-B3LYP and ωB97XD functionals provide a faithful prediction of the main UV–vis features of the complexes. The other examined functionals including dispersion (B3LYPD and B97D), Minnesota (M05-2X and M06), and long-range corrections (LC-BLYP) provide worse UV–vis spectral profiles than CAM-B3LYP (Supporting Information, Figure S2).

Raman Spectra. More structural details can be deduced from comparison of the experimental and theoretical Raman spectra. Similarly as for the UV–vis measurement shift of the Raman band 1511 cm^{-1} was used for the determination of optimal ligand/iron ratio (Supporting Information, Figure S3). The spectra stabilized for the ratio of about 16:1 (cf. the ratio 10:1 for UV–vis, see above).

The experimental Raman spectra indicate roughly (absolute Raman intensities cannot be directly measured; however, our

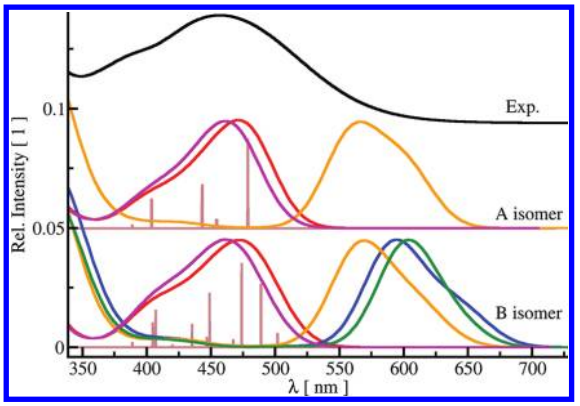

Figure 3. Experimental (black lines) and theoretical UV–vis spectra of the ferric complex of deferiprone (Figure 2). The DFT functionals were used with 6-311++G** basis set and CPCM model. Calculated intensities (line spectra) were broadened by Gaussian peaks with half-width 25 nm. B3LYP (blue lines), B3PW91 (orange lines), and CAM-B3LYP (red lines) spectra are displayed. CAM-B3LYP with MDF10 pseudopotential on iron, 6-31+G** basis set on other atoms, and CPCM model simulated the UV–vis most realistically (magenta lines). For the dark green line, the MDF10 pseudo potential (green lines) was imposed on iron atom of **B** isomer in the B3LYP functional. For CAM-B3LYP, individual transitions are plotted (vertical brown lines).

instrument setup ensures approximate stability of the cell position and the backscattered light collection) a 300× resonance enhancement of the signal when 3-hydroxy-4-pyridinone is complexed with the iron. The spectrum of the deferiprone complex was visible at ~100 times lower concentration for the deferiprone ligand. For example, in a detailed titration for the L:M ratio of 266 the intensities of free ligand (680 cm^{-1}) and the 1:3 complex (573 cm^{-1}) were almost equal, which would correspond to a 263× enhancement (Figure 4). The high absorbance of the solution observed during the measurement also indicates a resonance with an electronic state needed for the enhancement (Supporting

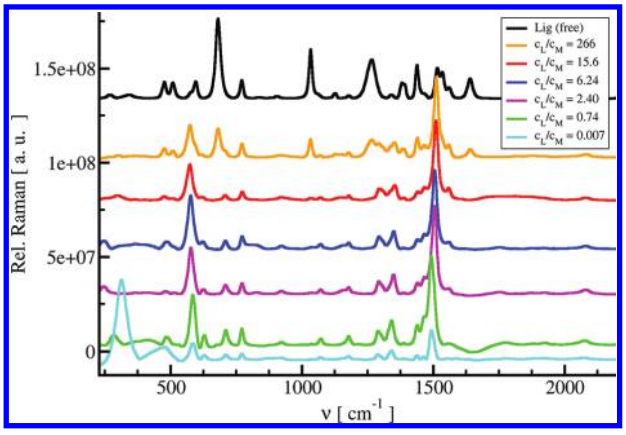

Figure 4. Titration of deferiprone with ferric chloride solution monitored by Raman spectroscopy. For the concentration ratio of 266, the intensities of free ligand (680 cm^{-1}) and the 1:3 complex (573 cm^{-1}) are almost equal. This approximately corresponds to 263 times enhancement of the Raman signal. The red spectrum (red lines) was selected as the best signal corresponding to the M:L 1:3 complex. The main bands maintained their positions while the ligand bands completely disappeared because of their relatively weak intensity in the preresonance.

dx.doi.org/10.1021/ic202004d | *Inorg. Chem.* 2012, 51, 4473–4481

Information, Figure S4). Because of the absorption of the laser light, the sample absorbance had to be kept below 2 to prevent sample overheating.

The resonance enhancement is enabled as a part of the experimental UV−vis spectrum is close to or even involves the laser excitation frequency of 532 nm (Figure 3; Supporting Information, Figure S4). The DFT computations all relatively faithfully reproduced the preresonance enhancement changes of the Raman scattering. As the CAM-B3LYP/6-311++G**/CPCM, ωB97XD/MDF10, 6-31+G**/CPCM, and CAM-B3LYP/MDF10, 6-31+G**/CPCM best reproduced the UV−vis pattern (Figure 3, Supporting Information, Figure S2), they were examined more closely for the Raman modeling. Note that correct Raman enhancement prediction is dependent on the correct transition energies visible in UV−vis. The Raman frequencies predicted with the 6-311++G** basis set were closer to experimental values than those predicted with the pseudopotential (cf. Supporting Information, Figure S5, red and green lines). On the other hand, the CAM-B3LYP/MDF10, 6-31+G**/CPCM model gave the ratio of intensities more realistically than the 6-311++G** basis set (Figure 5,

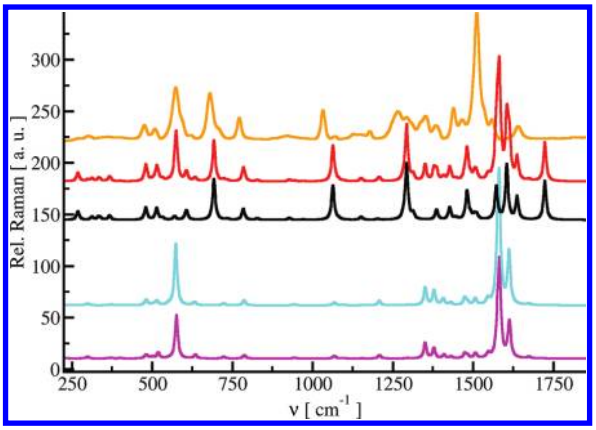

Figure 5. Experimental Raman spectrum of deferiprone/ferric ion mixture 266:1 (orange lines); simulated CAM-B3LYP/MDF10, 6-31+G**/CPCM spectrum of mixture deferiprone/**A** complex/**B** complex with ratio 650:0.61:0.39 (red lines); simulated spectrum of deferiprone (650× magnified, black lines), **A** complex (magenta lines) and **B** complex (cyan lines).

Supporting Information, Figure S6). The simulated enhancement is 1900× and 650× for the all-electron basis set and the pseudopotential with CAM-B3LYP, respectively. The ωB97XD/MDF10, 6-31+G**/CPCM computation provided enhancement of 1305× (Supporting Information, Figure S7). These values are larger, but qualitatively comparable to the experimental observation (263×, Figure 5, Supporting Information, Figure S6). As for UV−vis spectra simulation, CAM-B3LYP/MDF10, 6-31+G**/CPCM yielded the best prediction of the preresonance enhancement in Raman spectra. We consider such performance of the theoretical model to be quite reasonable, because of the steep intensity increase in the vicinity of the resonance[63] (see also Supporting Information, Figure S8).

Calculated vibrational frequencies of the two most intense peaks (experimentally at 1511 and 573 cm^{-1}) are listed in Table 2. Calculated frequencies of the second peak are almost insensitive to the solvent model, basis set, and the pseudo potential on the iron atom. The CAM-B3LYP functional predicted this vibration at the experimental position, whereas the largest error of 40−90 cm^{-1} was observed for the B97D functional.

Calculated normal-mode frequencies around 1511 cm^{-1} involving the conjugated system were less accurate. Among them, the most intense vibration at 1511 cm^{-1} was also very sensitive to the solvent model; the vacuum frequency could be significantly improved by application of CPCM. The pseudo potential provided almost the same results as the all-electron basis set on iron (cf. Table 2 items 4,5; 9,10; 14,15; and 17,18). The application of the full basis set (6-311++G**) on all atoms improved vibrational frequencies for examined functionals (B3LYP, B3PW91, and CAM-B3LYP). The predicted wavenumbers were even better than those predicted by the calculations with the relativistic pseudopotential on iron. The minor frequency changes correspond to the fact that the affected vibrations do not involve the motion of iron. On the other hand, the intensities are better described by the pseudopotential calculations. The best frequencies were obtained with the B3LYP functional (a 13 cm^{-1} error), the worst were again the B97D results (deviations of 160−200 cm^{-1} from the experiment). Although B3LYP functional did not predict correctly the resonance in the UV−vis calculation (Figure 3, blue line), it provides the best vibrational frequencies.

A closer examination of the experimental and computed vibrational frequencies of free ligand (Supporting Information, Table S1; Figure S9) and its ferric complex (Table 3) was performed with the 6-311++G** basis set and the CPCM solvent. Only bands which could be unambiguously assigned were considered.

The B3LYP functional provides the smallest standard deviation of the wavenumbers for the ligand (19 cm^{-1}), as well as, for the complex (13 cm^{-1}). The CAM-B3LYP functional results to the largest deviation of wavenumbers for both the ligand and complex. The CAM-B3LYP/MDF10/6-31+G** spectra could be significantly improved by scaling of the calculated frequencies.

The frequency changes are not significant enough to reliably distinguish the **A** and **B** (cf. Table 3, **A**, **B**, and the Boltzmann weighted sum). The root-mean-square errors are the same for **A** and **B**. For wavenumbers below 1250 cm^{-1} the B3PW91 functionals slightly favors the **A** isomer, whereas B3LYP and CAM-B3LYP do not indicate any preference.

The intensities are best reproduced with CAM-B3LYP (Figure 6), although frequencies above 1250 cm^{-1} calculated by this functional are systematically overestimated (by 20−50 cm^{-1}).

The DFT and experimental Raman intensities are consistent with an equilibrium between the **A** and **B** isomers in the sample, although the spectral differences are quite tiny. To investigate the intensity differences in detail, selected spectral parts calculated with the B3PW91 and CAM-B3LYP functionals with full basis set and the CAM-B3LYP functional with application of pseudopotential relativistic correction are magnified in Figures 7, 8, and 9, respectively.

The B3PW91 spectra indicate the existence of the **B** isomer by a more realistic ratio of intensities between the signals at 300 and 363 cm^{-1} (Figure 7). The same is true also for the ratio of intensities between 573 cm^{-1} and 620 cm^{-1}. In other regions, the **A** and **B** isomers cannot be distinguished.

The CAM-B3LYP calculation with full basis set (Figure 8) provides more contradictory results. The peak around 401 cm^{-1} can be better explained by the absence of the **B** isomer;

dx.doi.org/10.1021/ic202004d | Inorg. Chem. 2012, 51, 4473−4481

Table 2. Experimental and Calculated Vibrational Frequencies (cm^{-1}) of the Two Most Intense Raman Bands

item	method	isomer A		isomer B	
	B3LYP				
1	6-31+G**; Fe with 6-311++G**	1609	559	1605	557
2	6-31+G**; Fe with MDF10	1608	558	1605	556
3	all with 6-311++G**	1597	558	1593	556
4	6-31+G**; Fe with 6-311++G**, CPCM	1536	559	1534	556
5	6-31+G**; Fe with MDF10, CPCM	1536	559	1535	555
6	all with 6-311++G**, CPCM	1525	559	1524	556
	B3PW91				
7	6-31+G**; Fe with 6-311++G**	1631	562	1628	560
8	all with 6-311++G**	1620	562	1616	559
9	6-31+G**; Fe with 6-311++G**, CPCM	1557	562	1556	560
10	6-31+G**; Fe with MDF10, CPCM	1557	561	1557	558
11	all with 6-311++G** CPCM	1546	562	1545	559
	B97D				
12	6-31+G**; Fe with 6-311++G**	1335	532	1336	528
13	all with 6-311++G**	1325	530	1326	527
14	6-31+G**; Fe with 6-311++G**, CPCM	1324	532	1324	485
15	6-31+G**; Fe with MDF10, CPCM	1322	485	1347	496
16	all with 6-311++G**, CPCM	1314	532	1315	485
	CAM-B3LYP				
17	6-31+G**; Fe with 6-311++G**, CPCM	1581	577	1581	574
18	6-31+G**; Fe with MDF10, CPCM	1582	576	1581	573
19	all with 6-311++G**, CPCM	1570	577	1569	574
	B3LYPD				
20	6-31+G**; Fe with MDF10, CPCM	1536	560	1536	557
	M05-2X				
21	6-31+G**; Fe with MDF10, CPCM	1599	583	1601	581
	M06				
22	6-31+G**; Fe with MDF10, CPCM	1557	569	1555	567
	LC-BLYP				
23	6-31+G**; Fe with MDF10, CPCM	1643	594	1642	592
	ωB97XD				
24	6-31+G**; Fe with MDF10, CPCM	1587	580	1586	578
	experimental				
25		1511	573	1511	573

Table 3. Experimental and Computed (6-311++G**/CPCM) Wavenumbers (cm^{-1}) in the Deferiprone Complex

	functional								
	B3LYP			B3PW91			CAM-B3LYP		
experiment	A	B	[a]Sum	A	B	[a]Sum	A	B	[a]Sum
300	290	290	290	292	292	292	298	299	298
365	354	355	354	352	354	353	370	370	370
401	392	393	392	395	392	393	400	401	400
476	477	477	477	477	477	477	483	484	484
512	509	506	508	509	506	509	519	515	518
573	559	556	558	562	559	561	577	574	576
620	620	619	620	623	621	622	633	630	633
709	706	707	706	713	714	714	721	722	721
773	776	775	776	779	779	779	788	786	787
922	927	926	926	929	929	929	941	942	941
1071	1079	1078	1078	1081	1081	1081	1064	1064	1064
1179	1791	1791	1791	1194	1194	1194	1206	1206	1206
1294	1267	1268	1268	1278	1278	1278	1291	1291	1291
1352	1384	1381	1382	1348	1350	1349	1339	1340	1339
1511	1525	1524	1525	1546	1545	1546	1570	1569	1569
1559	1568	1567	1567	1586	1584	1585	1602	1601	1602
[b]STD	13	13	13	14	14	14	21	21	21

[a]Boltzmann averaged. [b]Standard deviation.

dx.doi.org/10.1021/ic202004d | Inorg. Chem. 2012, 51, 4473−4481

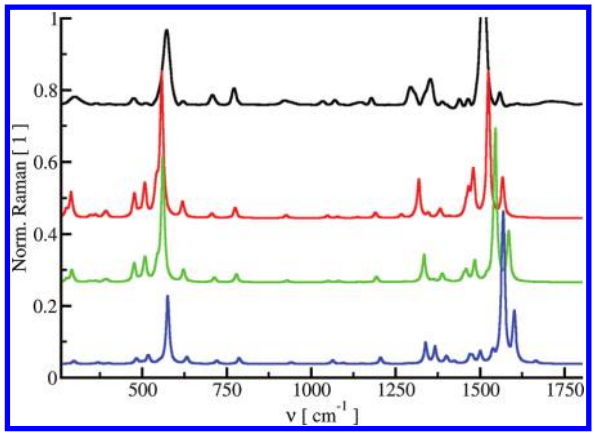

Figure 6. Experimental (black lines) and DFT/6-311++G** /CPCM (B3LYP, red lines; B3PW91, green lines; CAM-B3LYP, blue lines, Boltzmann-averaged) deferiprone complex Raman spectra.

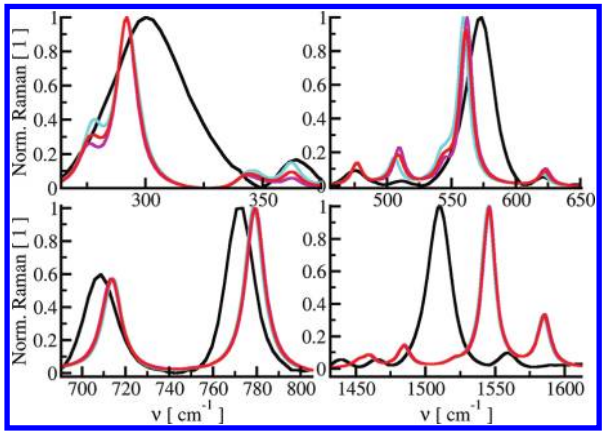

Figure 7. Experimental (black line) and B3PW91/6-311++G**/CPCM calculated spectra in selected spectral regions. **A** isomer (magenta lines), **B** isomer (cyan lines), Boltzmann average (red lines).

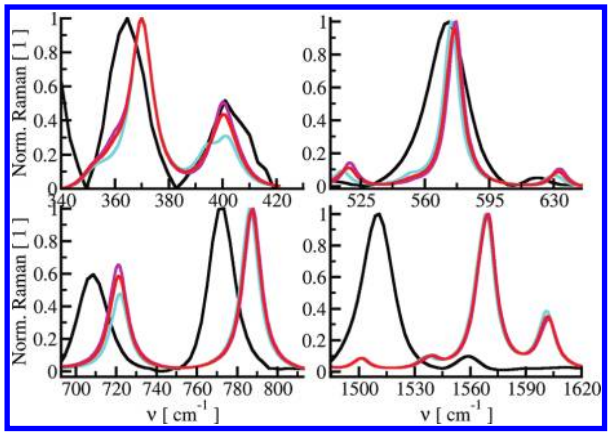

Figure 8. Experimental (black line) and CAM-B3LYP/6-311++G**/CPCM calculated spectra in selected regions. **A** isomer (magenta lines), **B** isomer (cyan lines), Boltzmann average (red lines).

however, the ratio between 573 cm^{-1} and 620 cm^{-1} indicated the presence of the **B** isomer, as it was in the case of the B3PW91 calculation. Moreover, the averaged spectra with Boltzmann's weights nicely simulate the peaks at 709 and 773 cm^{-1}.

The relativistic correction included in the pseudopotential calculation with CAM-B3LYP functional (Figure 9) indicated

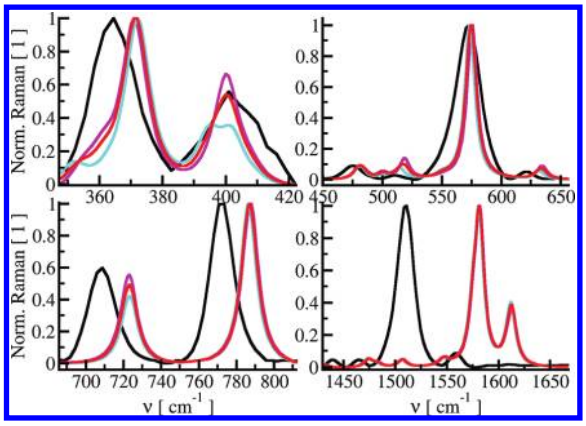

Figure 9. Experimental (black line) and CAM-B3LYP/MDF10 (Fe); 6-31+G** (other atoms)/CPCM calculated spectra in selected regions. **A** isomer (magenta lines), **B** isomer (cyan lines), Boltzmann average (red lines).

the existence of **B** isomer by comparison of the ratio of intensities between 573 cm^{-1} and 620 cm^{-1}, and between 363 cm^{-1} and 401 cm^{-1}. However, slight inconsistency is observed for wavenumbers 709 and 737 cm^{-1}, where the experimental spectrum is best simulated with the **A** isomer only.

The tiny differences between the simulated **A** and **B** isomers and their weighted sum indicate a presence of both isomers. The isomer equilibrium can also contribute to a broadening of measured peaks. In particular the simulations within around 573−620 cm^{-1} strongly support the argument, but for a more reliable determination of the conformer ratios higher experimental and theoretical accuracy is needed.

In the complex spectra, three marker peaks ("1", "2", and "3", Figure 10a,d) can be clearly distinguished, and assigned to normal mode vibrations. The first vibration (1) at 300 cm^{-1} involves motion of the iron (Figure 10, upper part). It is blue-shifted for the solvated ferric ion to 327 cm^{-1}. A bending of chelating oxygens contributes to the vibration (2) at 573 cm^{-1}. Finally, the most intense signal (3) at 1511 cm^{-1} is caused by aromatic C═C stretching. It is slightly red-shifted if compared to the free deferiprone (1516 cm^{-1}).

To investigate the stability of the marker vibrations in similar complexes, we measured also Raman spectra of the complexes of the Orn(2-methyl-3-hydroxy-4-pyridinone) and Lys(2-methyl-3-hydroxy-4-pyridinone) derivative (Figure 10b and c, respectively). Clearly, the frequencies and relative intensities of the characteristic vibrations are similar. This can be explained by their localization close to the ferric ion binding site in the 3-hydroxy-4-pyridinone ring, not much influenced by the substituents. The simpler deferiprone thus appears as a realistic model of the iron binding in other peptide conjugates, at least for the purpose of the Raman spectroscopy.

■ CONCLUSION

Our results showed that the ferric complex of deferiprone was a suitable model for UV−vis and Raman spectroscopic studies of 3-hydroxy-4-pyridinones and their conjugates with amino acids and peptides.

The DFT computations of relative conformer energies indicated a conformer equilibrium, which could contribute to the broadening of experimental Raman intensities. For a reliable quantitative resolution from the spectra, however, a

dx.doi.org/10.1021/ic202004d | Inorg. Chem. 2012, 51, 4473−4481

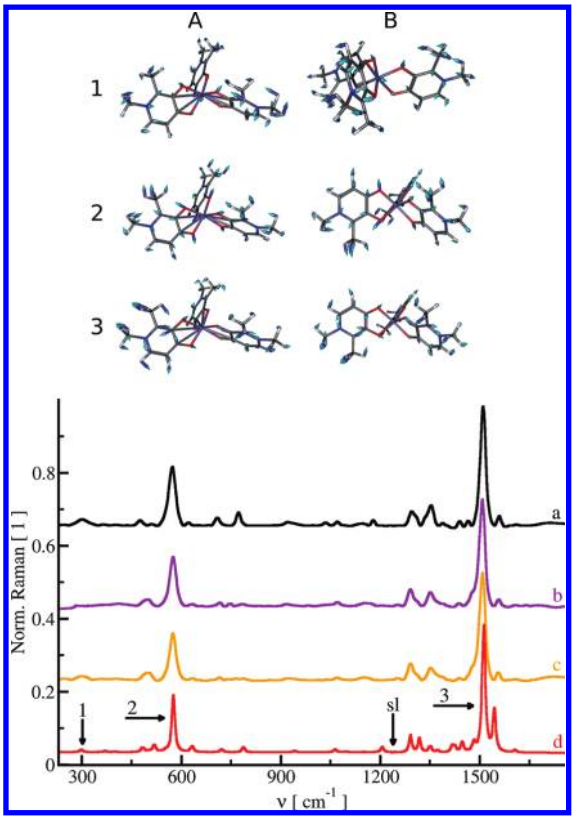

Figure 10. Raman spectra of ferric complexes: (a) experiment and (d) calculation for deferiprone and (b, c) experiments for Orn and Lys conjugates with 3-hydroxy-4-pyridinone, respectively. Numbers 1, 2, and 3, indicate the vibrations displayed above involving the iron, chelating oxygens, and aromatic carbons, respectively. The "sl" indicates the scaling limit at 1250 cm^{-1}. Frequencies above the scaling limit were multiplied by 0.946.

higher accuracy of the experiments and computations would be needed.

For the Raman intensities, three important vibrational frequencies were identified, including the central metal atom, characteristic for the complexation. The Raman spectra could be predicted with approximately the same accuracy using the B3LYP, B3PW91, or CAM-B3LYP functionals. For UV−vis spectra simulation, the CAM-B3LYP and ωB97XD functionals with CPCM model provided the best results, although the spectra were not sensitive to the complex geometry. Only the CAM-B3LYP and ωB97XD results were consistent both for Raman and for UV−vis modeling, because of the preresonance enhancement of the Raman signal in the complex. For frequencies above 1200 cm^{-1} including vibrations of the polar group, the usage of the solvent model was critical for the faithful reproduction of the spectra.

The combined computational and spectroscopic approach proved to be useful to study the ferric complex structures. In the future, higher precision of the DFT simulation and experiment and reliable MD force fields allowing the inclusion of explicit hydration are desirable.

■ ASSOCIATED CONTENT

Supporting Information

Analyses of the dependency of spectral properties on ligand-to-metal ratio, calculated UV−vis spectra with various functionals, absorbance of laser light during Raman measurements, calculated Raman spectra with various functionals, calculated preresonance Raman spectra with various excitation wavelength, experimental and calculated spectra of deferiprone, selection of spin state, and geometries of optimized complexes. This material is available free of charge via the Internet at http://pubs.acs.org.

■ AUTHOR INFORMATION

Corresponding Author

*Phone: +420-220183445. Fax.: +420-233335268. E-mail: jsebestik@seznam.cz.

Notes

The authors declare no competing financial interest.

■ ACKNOWLEDGMENTS

The work was supported by GA ČR (203/07/1517, P208/11/0105), AS (M200550902), and MŠMT (LH11033).

■ REFERENCES

(1) Liu, Z. D.; Hider, R. C. *Med. Res. Rev.* **2002**, *22*, 26.
(2) Hider, R. C.; Ma, Y.; Molina-Holgado, F.; Gaeta., A.; Roy, S. *Biochem. Soc. Trans.* **2008**, *36*, 1304.
(3) Gaeta, A.; Molina-Holgado, F.; Kong, X. L.; Salvage, S.; Fakih, S.; Francis, P. T.; Williams, R. J.; Hider, R. C. *Bioorg. Med. Chem.* **2011**, *19*, 1285.
(4) Silvestri, L.; Camaschella, C. *J. Cell. Mol. Med.* **2008**, *12*, 1548.
(5) Singh, A.; Kong, Q.; Luo, X.; Petersen, R. B.; Meyerson, H.; Singh, N. *PLoS One* **2009**, *4*, e6115.
(6) Fenton, H. J. H. *J. Chem. Soc., Trans.* **1894**, *65*, 899.
(7) Liu, Z. D.; Hider, R. C. *Coord. Chem. Rev.* **2002**, *232*, 151.
(8) Qiu, D.-H.; Huang, Z.-L.; Zhou, T.; Shen, C.; Hider, R. C. *FEMS Microbiol. Lett.* **2011**, *314*, 107.
(9) Katoh, A.; Hikita, Y.; Harata, M.; Ohkanada, J.; Tsubomura, T.; Higuchi, A.; Saito, R.; Harada, K. *Heterocycles* **2001**, *55*, 2171.
(10) Grazina, R.; Gano, L.; Šebestík, J.; Santos, M. A. *J. Inorg. Biochem.* **2009**, *103*, 262.
(11) Šebestík, J.; Niederhafner, P.; Ježek, J. *Amino Acids* **2011**, *40*, 301.
(12) Kong, X.; Neubert, H.; Zhou, T.; Liu, Z. D.; Hider, R. C. *J. Mass Spectrom.* **2008**, *43*, 617.
(13) Zhou, T.; Neubert, H.; Liu, D. Y.; Liu, Z. D.; Ma, Y. M.; Kong, X. L.; Luo, W.; Mark, S.; Hider, R. C. *J. Med. Chem.* **2006**, *49*, 4171.
(14) Walker, F. A. *Inorg. Chem.* **2003**, *42*, 4526.
(15) Barron, L. D.; Buckingham, A. D. *Chem. Phys. Lett.* **2010**, *492*, 199.
(16) Wolny, J. A.; Paulsen, H.; Trautwein, A. X.; Schünemann, V. *Coord. Chem. Rev.* **2009**, *253*, 2423.
(17) Yamamoto, S.; Straka, M.; Watarai, H.; Bouř, P. *Phys. Chem. Chem. Phys.* **2010**, *12*, 11021.
(18) Xiao, G.; van der Helm, D.; Hider, R. C.; Rai, B. L. *J. Phys. Chem.* **1996**, *100*, 2345.
(19) Harris, D.; Loew, G. H. *J. Phys. Chem. A* **1997**, *101*, 3959.
(20) Jarzecki, A. A.; Anbar, A. D.; Spiro, T. G. *J. Phys. Chem. A* **2004**, *108*, 2726.
(21) Dey, A.; Solomon, E. I. *Inorg. Chim. Acta* **2010**, *363*, 2762.
(22) Chaudhary, A.; Patra, R.; Rath, S. P. *Eur. J. Inorg. Chem.* **2010**, *2010*, 5211.
(23) Brewer, G.; Brewer, C.; White, G.; Butcher, R. J.; Viragh, C.; Carpenter, E. E.; Schmiedekamp, A. *Inorg. Chim. Acta* **2009**, *362*, 4158.
(24) Olah, J.; Harvey, J. N. *J. Phys. Chem. A* **2009**, *113*, 7338.
(25) Ohrstrom, L.; Michaud-Soret, I. *J. Phys. Chem. A* **1999**, *103*, 256.
(26) Soldatova, A. V.; Ibrahim, M.; Olson, J. S.; Czernuszewicz, R. S.; Spiro, T. G. *J. Am. Chem. Soc.* **2010**, *132*, 4614.
(27) Griffith, W. P.; Mostafa, S. I. *Polyhedron* **1992**, *11*, 2997.
(28) Yamamoto, S.; Watarai, H.; Bouř, P. *ChemPhysChem* **2011**, *12*, 1509.

(29) Buděšínský, M.; Daněček, P.; Bednárová, L.; Kapitán, J.; Baumruk, V.; Bouř, P. *J. Phys. Chem. A* **2008**, *112*, 8633.
(30) Šebestík, J.; Bouř, P. *J. Phys. Chem. Lett.* **2011**, *2*, 498.
(31) Green, D. E.; Ferreira, C. L.; Stick, R. V.; Patrick, B. O.; Adam, M. J.; Orvig, C. *Bioconjugate Chem.* **2005**, *16*, 1597.
(32) Dobbin, P. S.; Hider, R. C.; Hall, A. D.; Taylor, P. D.; Sarpong, P.; Porter, J. B.; Xiao, G.; van der Held, D. *J. Med. Chem.* **1993**, *36*, 2448.
(33) Liu, G.; Miller, S. C.; Bruenger, F. W. *Synth. Commun.* **1995**, *25*, 3247.
(34) Rumbo, A.; Mourino, A.; Castedo, L.; Mascarenas, J. L. *J. Org. Chem.* **1996**, *61*, 6114.
(35) Santos, M. A.; Gil, M.; Gano, L.; Chaves, S. *J. Biol. Inorg. Chem.* **2005**, *10*, 564.
(36) Frisch, M. J.et al. *Gaussian 09*, Revision A.1; Gaussian, Inc.: Wallingford, CT, 2009.
(37) Becke, A. D. *J. Chem. Phys.* **1993**, *98*, 5648.
(38) Vosko, S. H.; Wilk, L.; Nusair, M. *Can. J. Phys.* **1980**, *58*, 1200.
(39) Lee, C.; Yang, W.; Parr, R. G. *Phys. Rev. B* **1988**, *37*, 785.
(40) Miehlich, B.; Savin, A.; Stoll, H.; Preuss, H. *Chem. Phys. Lett.* **1989**, *157*, 200.
(41) Perdew, J. P.; Burke, K.; Wang, Y. *Phys. Rev. B* **1996**, *54*, 16533.
(42) Perdew, J. P.; Chevary, J. A.; Vosko, S. H.; Jackson, K. A.; Pederson, M. R.; Singh, D. J.; Fiolhais, C. *Phys. Rev. B* **1992**, *46*, 6671.
(43) Grimme, S. *J. Comput. Chem.* **2006**, *27*, 1787.
(44) Yanai, T.; Tew, D.; Handy, N. *Chem. Phys. Lett.* **2004**, *393*, 51.
(45) Grimme, S. *J. Comput. Chem.* **2004**, *25*, 1463.
(46) Grimme, S. *J. Comput. Chem.* **2006**, *27*, 1787.
(47) Zhao, Y.; Schultz, N. E.; Truhlar, D. G. *J. Chem. Theory Comput.* **2006**, *2*, 364.
(48) Zhao, Y.; Truhlar, D. G. *Theor. Chem. Acc.* **2008**, *120*, 215.
(49) Iikura, H.; Tsuneda, T.; Yanai, T.; Hirao, K. *J. Chem. Phys.* **2001**, *115*, 3540.
(50) Chai, J.-D.; Head-Gordon, M. *Phys. Chem. Chem. Phys.* **2008**, *10*, 6615.
(51) Chai, J.-D.; Head-Gordon, M. *J. Chem. Phys.* **2008**, *128*, 084106.
(52) Hurley, M. M.; Pacios, L. F.; Christiansen, P. A.; Ross, R. B.; Ermler, W. C. *J. Chem. Phys.* **1986**, *84*, 6840.
(53) Dolg, M.; Wedig, U.; Stoll, H.; Preuss, H. *J. Chem. Phys.* **1987**, *86*, 866.
(54) Metz, B.; Stoll, H.; Dolg, M. *J. Chem. Phys.* **2000**, *113*, 2563.
(55) Barone, V.; Cossi, M. *J. Phys. Chem. A* **1998**, *102*, 1995.
(56) Cossi, M.; Rega, N.; Scalmani, G.; Barone, V. *J. Comput. Chem.* **2003**, *24*, 669.
(57) Tomasi, J.; Mennucci, B.; Cammi, R. *Chem. Rev.* **2005**, *105*, 2999.
(58) Klamt, A.; Schüürmann, G. *J. Chem. Soc., Perkin Trans. 2* **1993**, 799.
(59) Kandioller, W.; Kurzwernhart, A.; Hanif, M.; Meier, S. M.; Henke, H.; Keppler, B. K.; Hartinger, C. G. *J. Organomet. Chem.* **2011**, *696*, 999.
(60) Charalambous, J.; Dodd, A.; McPartlin, M.; Matondo, S. O. C.; Pathirana, N. D.; Powell, H. R. *Polyhedron* **1988**, *7*, 2235.
(61) Šebek, J.; Gyurcsik, B.; Šebestík, J.; Kejík, Z.; Bednárová, L.; Bouř, P. *J. Phys. Chem. A* **2007**, *111*, 2750.
(62) Šebek, J.; Bouř, P. *J. Phys. Chem. A* **2006**, *110*, 4702.
(63) Barron, L. D. *Molecular light scattering and optical activity*; Cambridge University Press: Cambridge, U.K., 2004.